Combustion and Flame 159 (2012) 577–590

Contents lists available at SciVerse ScienceDirect

Combustion and Flame

journal homepage: www.elsevier.com/locate/combustflame

Measurement of laminar burning velocity and Markstein length relative to fresh gases using a new postprocessing procedure: Application to laminar spherical flames for methane, ethanol and isooctane/air mixtures

Emilien Varea, Vincent Modica *, Alexis Vandel, Bruno Renou

CORIA – CNRS UMR 6614, Université et INSA de Rouen, site universitaire du Madrillet, 76801 Saint-Etienne du Rouvray cedex, France

ARTICLE INFO

Article history:
Received 14 April 2011
Received in revised form 2 September 2011
Accepted 5 September 2011
Available online 14 October 2011

Keywords:
Laminar burning velocity
Markstein length
Outwardly expanding flame
Ethanol
Isooctane
Methane

ABSTRACT

The purpose of this study is to present a new tool for extracting the laminar burning velocity in the case of spherically outward expanding flames. This new procedure makes it possible to determine the laminar burning velocity directly based on the flame displacement speed and the global fresh gas velocity near the preheat zone of the flame front. It therefore presents a very interesting alternative to the standard method (commonly used in the literature), which is based on the flame front displacement and the ratio of unburned and burned gas densities. The influence of external flame stretching on the burning velocity can be characterized and the Markstein length relative to the unburned gases (i.e., fresh gases) can be deduced by using this new tool. Contrary to the standard procedure, the unstretched laminar burning velocity is determined directly without using the fuel mixture properties. The temporal evolution of the flame front is visualized by high-speed laser tomography and the algorithm, based on a tomographic image correlation method, makes it possible to accurately measure the fresh gas velocity near the preheat zone of the flame front. The measurements of laminar flame speeds are carried out in a high-pressure and high-temperature constant-volume vessel over a wide range of equivalence ratios for methane, ethanol, and isooctane/air mixtures. To validate the experimental facility and the postprocessing of the flame images, fresh gas velocities and unstretched laminar burning velocities, as well as Markstein lengths relative to burned and unburned gases, are presented and compared with experimental and numerical results of the literature for methane/air flames. New results concerning ethanol/air and isooctane/air flames are presented for various experimental conditions (373 K, equivalence ratios range 0.7–1.5, pressure range 0.1–5 MPa).

1. Introduction

The laminar burning velocity plays an important role in studying the combustion process because it contains fundamental information regarding the reactivity, diffusivity, and exothermicity of a combustible mixture. In automotive engineering, knowledge of the unstretched laminar burning velocity provides the information necessary to estimate the fuel-burning rate in spark-ignition (SI) engines, as well as the engine's efficiency and its exhaust gas emissions. The ability to produce accurate measurements of the laminar burning velocity is also essential for turbulent combustion modeling and the validation of chemical kinetic mechanisms for conventional and alternative fuels, as well as for the understanding of the combustion process at high pressure and temperature.

At present, experimental measurements of burning velocity are increasingly applied to biofuels such as ethanol, which is widely used in the automotive industry (either pure or blended with gasoline or diesel fuels). When used in internal combustion engines, ethanol leads to an increase in the octane number of the blended fuel, resulting in the ability to increase the compression ratio and the engine's performance. The effect of ethanol on pollutant emissions is varying and depends on the fuel blend: in the case of ethanol–gasoline fuel blends, engine tests indicated that carbon monoxide (CO) and unburned hydrocarbon (HC) emissions decrease as a result of the leaning effect caused by the ethanol addition [1]. However, the results are different for ethanol–diesel fuel blends: CO and HC emissions increase and depend on ethanol blending ratio and engine operating conditions (injection timing, engine load) [2]. In diesel engines, ethanol blending reduces particulate matter also.

There is much demand for chemical kinetic mechanisms that are capable of representing a wide range of ethanol–gasoline blends. The use of experimental measurements of the unstretched laminar burning velocity to optimize these mechanisms is therefore very advantageous. In the present paper, the primary reference fuel isooctane is used as a surrogate component of gasoline.

* Corresponding author.
E-mail address: vincent.modica@coria.fr (V. Modica).

0010-2180/$ - see front matter © 2011 The Combustion Institute. Published by Elsevier Inc. All rights reserved.
doi:10.1016/j.combustflame.2011.09.002

Nomenclature

k	flame stretch rate (s^{-1})
L_u	unburned gas Markstein length (mm)
L_b	burned gas Markstein length (mm)
P	pressure (MPa)
r	flame radius (cm)
s	laminar flame speed (cm s^{-1})
s^0	unstretched laminar flame speed (cm s^{-1})
T	temperature (K)
u_n	laminar burning velocity (cm s^{-1})
u_n^0	unstretched laminar burning velocity (cm s^{-1})
u_s^0	unstretched laminar burning velocity in the case of adiabatic condition (cm s^{-1})
u_g^*	fresh gas velocity along the normal to the flame front (cm s^{-1})
u^g	fresh gas velocity at the entrance of the flame front (cm s^{-1})
ρ_b	burned gases density (kg m^{-3})
ρ_u	unburned gases density (kg m^{-3})
Φ	equivalence ratio

The laminar burning velocity can be determined via several experimental approaches using different flame configurations such as spherical expanding flames using closed vessels [3–25], counterflow or stagnation flames [26–30], burner flat flames stabilized using the heat flux method [31–36], and Bunsen flames [37–39]. Among these various techniques, the spherically outward expanding flame configuration shows greater similarity to flame propagation in spark-ignition engines and enables us to reach thermodynamic conditions (elevated pressures and temperatures) close to those encountered in internal combustion (IC) engines. These experimental conditions are very difficult to reach using steady-state methods (flat flame burner, rim-stabilized conical flame, counterflow), which have operational ranges limited to a few atmospheres due to flame stability problems [12].

In the case of spherically expanding flames, two different formulations are generally presented to calculate the unstretched laminar burning velocity: the burning velocity can either be estimated from the displacement of the flame front and the ratio of unburned and burned gas densities [40] or determined directly from the difference between the flame propagation speed and the fresh gas velocity [40–42].

The first method is the one most commonly employed in previous works [3–24] using spherically expanding flame configurations. This method, which is based on the rate appearance of burned gas (expressed by the flame speed), describes the dynamic expansion of the burned gas behind the flame front, the temporal evolution of which is recorded by Schlieren or shadow photography with a high-speed camera. Theoretical and experimental studies have proposed different models based on linear [43] or nonlinear [44–47] relationships between the flame propagation speed and the flame stretch rate. The sensitivity of the flame propagation to the stretch rate is characterized by a constant, the burned gas Markstein length, L_b, whose values are widely detailed in the literature for many fuel mixtures. However, the sensitivity of the burning velocity, u_n, in relation to the flame stretch rate cannot be described by this approach.

To extract the unstretched burning velocity, u_n^0, using this method, the flame speed must be linearly or nonlinearly extrapolated to a zero stretch rate and it must be divided by the ratio of unburned and burned gas densities at chemical equilibrium for an adiabatic combustion. Therefore, this last expression is dependent on the physicochemical properties of the burning mixture which that are estimated using several assumptions: perfect gases, isobaric, adiabatic, and equilibrium conditions. These strong assumptions may be valid not always and especially for fuel blends such as isooctane–ethanol or for hydrocarbon mixtures diluted by components like carbon dioxide (CO_2), carbon monoxide (CO), and water vapor (H_2O), which have strong spectral radiation absorption. Because of the thermal, transport, and chemical effects of these components on the combustion mechanism, the real flame temperature differs from the adiabatic temperature and thus the unstretched burning velocity, calculated using adiabatic assumptions, is erroneous. For example, in the case of CH_4/CO_2 planar propagating flames, the computational study of Yu et al. [48] shows that radiation absorption leads to a higher flame temperature and a higher burning velocity than in the case of the adiabatic flame.

The second method used to extract the unstretched burning velocity is based on the rate of disappearance of cold unburned gas and depends on two factors: the entrainment of cold unburned gas by the flame front (expressed by the fresh gas velocity) and the expansion of completely burned gas behind the flame front (expressed by the flame speed). The difference between flame speed and fresh gas velocity allows us to determine the laminar burning velocity accurately without using the properties of the fuel mixture, and it enables us to relate the burning velocity to the flame stretch rate. In this case, the influence of external stretching on the burning velocity is characterized by the Markstein length relative to the unburned gases (i.e., fresh gases), L_u. It is very important to know the values of the unburned gas Markstein length and the laminar burning velocity in turbulent combustion modeling because the sensitivity of the burning velocity (or the burning rate) and its relation to flame stretch can be directly characterized. But in the case of spherically expanding flames, very few studies [41,42,49] have experimentally determined both of these thermophysical parameters. The reason for this omission is that the principal difficulty of this technique lies with the accuracy of the fresh gas velocity measurement near the preheat zone of the flame front, whose thickness is less than a millimeter. One of the main objectives of the present study is to propose an algorithm to postprocess high-speed tomographic recordings to simultaneously achieve a measurement of the flame speed and of the fresh gas velocity at the entrance of the flame front. The laminar burning velocity, u_n, is extracted from both of these quantities (depending on the global flame stretch). Values of the unburned gas Markstein length, L_u, and unstretched burning velocity, u_n^0, are extrapolated using linear and nonlinear methods.

To test the validity of this new procedure, the measurements are applied to methane/air flames over a broad range of equivalence ratios (0.6–1.2) at atmospheric pressure (0.1 MPa) and at ambient temperature (298 K). Values of unstretched burning velocity and burned gas Markstein length, L_b, calculated with both formulations are compared to experimental and numerical results from the literature. To conclude, values of unburned gas Markstein length, L_u, are detailed for these experimental conditions. In a second part of this paper, this new procedure is applied to isooctane and ethanol/air flames, for which very few data are available in the literature for the following experimental conditions: 373 K, an equivalence ratio range of 0.7–1.5 and a pressure range of 0.1–5 MPa.

2. Experimental apparatus

To measure the laminar burning velocity, experiments are conducted in a high-pressure and high-temperature constant–volume vessel (Fig. 1), equipped with different sensors and an optical system.

2.1. High-pressure and high-temperature facility

The experimental facility enables us to reach thermodynamic conditions close to those encountered in internal combustion engines; the maximum operating pressure is limited to 2 MPa and the maximum temperature is 573 K. The radius of the inner chamber is 85 mm and the inner volume of the stainless steel combustion chamber is 2.6 l. Two types of fuels, gaseous or liquid, can be used in this experimental device. Fuels that are gaseous under ambient conditions are charged directly from bottles through mass controllers. Liquid fuels are first vaporized in a heated chamber by using a "controlled evaporator mixer (CEM)" (*Bronkhorst*) and then charged through heated lines into the vessel. During the experiments, the liquid fuel vaporization system showed no coking inside the vaporization chamber, no recondensation, and no flow rate oscillation. To obtain a homogeneous mixture, all gases are premixed in a tank before injection into the combustion chamber and the equivalence ratio of the mixture is measured and regulated by Coriolis or thermal mass flow controllers connected to a computer. An electrical heating system, which is monitored by a proportional integral derivative (PID) controller, regulates the temperature of the mixing tank and of the combustion chamber. The temperature is controlled inside the chamber by two thermocouples that ensure uniformity of the temperature field. The compressed fuel/air mixture is supplied continuously from the bottom of the combustion chamber. The pressure level, which is checked in the vessel with a piezoelectric pressure sensor, is kept constant by adjusting the control valve. Once both the composition of the fuel mixture and the thermodynamic conditions are achieved and unchanging, two stop valves are used to close the combustion chamber. Ignition takes place 1 min later to avoid any flow perturbation during the flame propagation. The combustible mixture is spark-ignited at the center of this chamber by two stainless steel electrodes linked to a capacitive discharge ignition system using minimum spark energies to avoid ignition disturbances. The electrode diameter is 0.5 mm and the gap between electrodes is kept constant of 1.5 mm. During the combustion process, the evolution of the chamber pressure is acquired by a dynamic pressure transducer (Kistler). Once combustion is complete, the chamber is ventilated and purged with nitrogen to remove condensed water vapor.

2.2. Optical diagnostics

The chamber is equipped with three transparent windows for optical diagnostics. Flame speed and fresh gas velocity are obtained from high-speed laser tomography recordings. A double cavity Nd:YLF laser (Darwin Dual, Quantronix), delivering pulses of 6 mJ at 527 nm and at 5 kHz, is used to illuminate seeding particles. The laser sheet is created by associating one cylindrical lens of focal length – 13 mm and one spherical lens of focal length 254 mm. A high-speed camera (Photron Fastcam SA1.1) records an 8-bit image couple of 1024 × 1024 pixels at a frequency of 5 kHz. The camera, which is mounted with a 105-mm macro-Nikon lens (f/2.8), has a field of view of 50.2 × 50.2 mm^2, which leads to a magnification ratio of 0.049 mm/pixels. An interferential pass band filter (527 ± 10 nm) is used to remove the flame chemiluminescence. To capture the tomography images, the chamber is seeded with silicone oil droplets (Rhodorsil), which vaporize at an isotherm of about 580 K. This boiling point temperature is high enough for the seeding droplets to exist well into the preheat zone and can be used to capture the minimum velocity point upstream of the flame. The seeding particles do not survive in the postflame zone; nevertheless this type of silicone fluid does not have any observable effect on the flame. Several tests with different seeding particle concentrations have shown that the effect of particle concentration on the measured flame speed is quite no-insignificant. This finding has been verified for the experimental conditions that are detailed in our study.

2.3. Experimental conditions

To exclude the influence of the ignition energy [40] and the chamber confinement effects, only spherical flame images with ra-

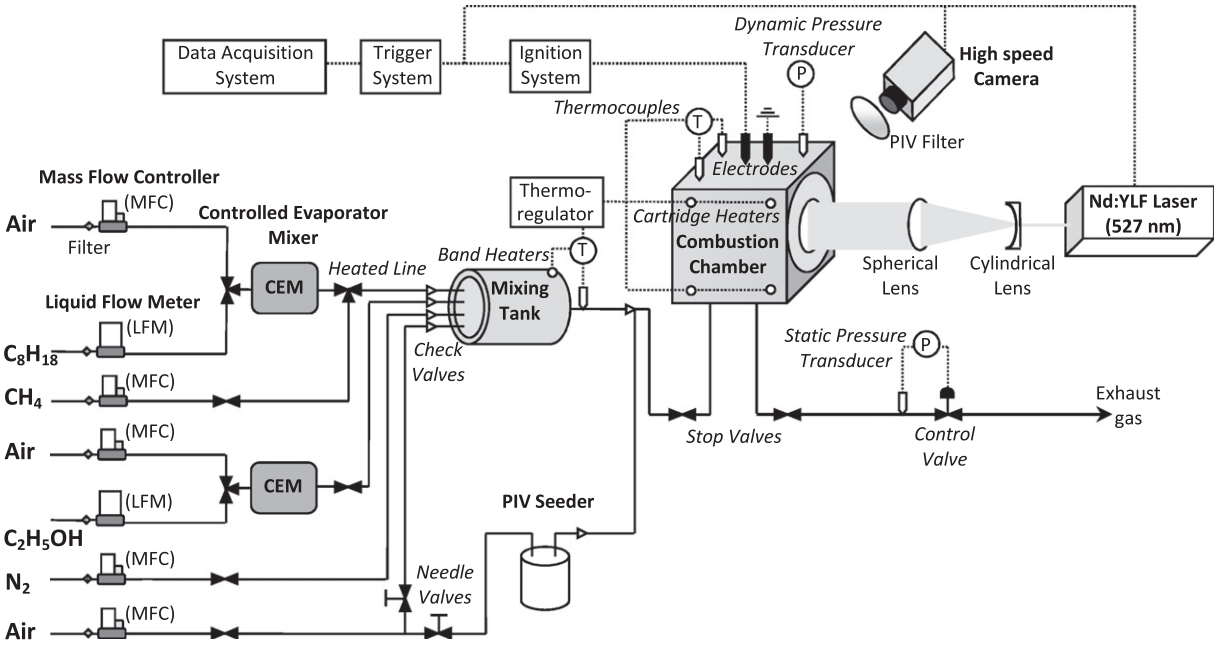

Fig. 1. Experimental setup.

Table 1
Experimental conditions.

	Equivalence ratio Φ	Pressure P (MPa)	Temperature T (K)
Methane CH_4	0.6–1.3	0.1	298
Ethanol C_2H_5OH	0.7–1.5	0.1–0.5	373
Isooctane C_8H_{18}	0.8–1.4	0.1	373

dii larger than 6.5 mm and smaller than 19 mm were used to determine the flame speeds. This value of 19 mm corresponds to a flame radius that is approximately 22% of the radius of the inner chamber. The effect of confinement can be neglected for flame radii of less than 30% of the wall radius, based on results of Burke et al. [5]. Moreover, within this region, dynamic pressure measurements and temperature measurements show that the total chamber pressure, as well as the temperature ahead of the flame, can be considered constant and to be those of the initial state. Laminar burning-velocity measurements are performed for methane, ethanol, and isooctane/air mixtures. Table 1 summarizes the ranges of equivalence ratios Φ, pressure P, and temperature T that we tested in this study. Throughout the experiments, these parameters are measured with the following uncertainties: $\Delta T/T = 0.5\%$ (thermocouple accuracy), $\Delta P/P = 0.5\%$ (pressure sensor accuracy), and $0.056\% < \Delta\Phi/\Phi < 0.07\%$ (mass flow controller accuracy). For each experimental condition, experiments were performed five times and all values of laminar burning velocity and Markstein length presented in this paper are averages based on this series of five experiments.

3. Laminar burning speed extraction and Markstein lengths

In the case of a spherically expanding flame at constant pressure, two methods are used to extract the laminar burning velocity.

3.1. First approach (developed in this work)

The first approach to extracting the burning velocity is based on the rate of disappearance of cold, unburned gas. It involves the knowledge of two factors:

- The rate of entrainment of cold unburned gas by the flame front (expressed by the fresh gas velocity at the entrance of the flame front, u_g).
- The temporal evolution of the flame front (expressed by the flame speed, s).

The laminar burning velocity, u_n, is directly determined by the flame speed and the fresh gas velocity at the entrance of the flame front using the following expression [40,41]:

$$u_n = S - u_g. \tag{1}$$

In the case of a spherically outward expanding flame, the flame speed, s, is defined as the temporal derivative of the flame radius evolution, $r(t)$:

$$S = \frac{dr}{dt}. \tag{2}$$

During this temporal evolution, the flame front is affected by the stretch rate, k, which influences the flame dynamic and which is expressed, in the case of a spherically expanding flame front, as follows:

$$K = \frac{2}{r}\cdot\frac{dr}{dt} = \frac{2}{r}\cdot S. \tag{3}$$

Asymptotic developments have initially shown a nonlinear relationship between the flame stretch rate and the laminar burning velocity [50],

$$\left(\frac{u_n}{u_n^0}\right)^2 \cdot In\left(\left(\frac{u_n}{u_n^0}\right)^2\right) = -\frac{2\cdot L_u\cdot k}{u_n^0}, \tag{4}$$

where u_n^0 is the unstretched laminar burning velocity and L_u is the Markstein length relative to the unburned gases (i.e., fresh gases). This length scale is very important in combustion because it can directly characterize the flame response (in terms of reaction rate) to the flame stretch. Within the limits of weakly stretched flames, the ratio (u_n/u_n^0) is close to unity and the following linear relationship between flame stretch and burning velocity can be obtained:

$$u_n = u_n^0 - L_u\cdot k. \tag{5}$$

In this study, both methods (linear and nonlinear) will be applied to flame images. Results in terms of unburned gas Markstein length and unstretched laminar burning velocity will be compared. Measurements of the unstretched laminar burning velocity will be compared with results obtained via the second approach based on flame speed evolution.

3.2. Second approach (most commonly used in the literature)

In the second method, the flame speed is related to the flame stretch rate through a nonlinear relationship [44]:

$$\left(\frac{S}{S^0}\right)^2 \cdot In\left(\left(\frac{S}{S^0}\right)^2\right) = \frac{2\cdot L_b\cdot k}{S^0}, \tag{6}$$

where s^0 is the unstretched flame speed and L_b is the burned gas Markstein length. Far from the extinction limit, the ratio (s/s^0) is close to unity and the linear model initially proposed by Clavin [43] is retrieved:

$$S = S^0 - L_b\cdot k. \tag{7}$$

The unstretched flame speed, s^0, is extrapolated as follows:

$$S^0 = \lim_{k\to 0}\left(\frac{dr}{dt}\right). \tag{8}$$

Depending on the experimental conditions (flame affected or not by stretch, Lewis number of the fuel/air mixture, range of equivalence ratios), the linear method will result in an overprediction of the unstretched flame speed [44–47], in which case the nonlinear method must be applied to extrapolate this quantity. For constant-pressure flame propagation, the unstretched laminar burning velocity, u_n^0, can be extracted from the unstretched flame speed, s^0, and from the density ratio using the approximation

$$u_n^0 \cong u_s^0 = \frac{\rho_b}{\rho_u}\cdot S^0, \tag{9}$$

where ρ_b and ρ_u are the densities of the adiabatically burned gas and the unburned gas, respectively. The density ratio is dependent on the burned-to-unburned gas temperature ratio, and the burned gas temperature is estimated for adiabatic conditions. Thereby, u_s^0 is the unstretched laminar burning velocity calculated for adiabatic, isobaric and perfect gas conditions. For some experimental conditions (blended fuels, effects of radiation absorption in CO_2^- or H_2O-diluted flames), the real flame temperature can differ from the adiabatic temperature and thus the unstretched laminar burning velocity calculation may be inaccurate if we use the expression (9). Moreover, the linear or nonlinear extraction of the unstretched flame speed also affects the values of the unstretched burning velocity. This definition is the one most commonly employed in the literature [3–24] to calculate the unstretched burning velocity.

It is based on the rate of formation of burned gases and it describes their dynamic expansion behind the flame front (the displacement of which is usually visualized by laser tomography or the Schlieren method). Using this second approach, the influence of stretch on the flame response is expressed by the Markstein length relative to burned gases, but contrary to the first method, the definition (9) is not capable of characterizing the sensitivity of the burning rate as it relates to the flame stretch. The advantage of the first approach is its ability to determine the Markstein length relative to fresh gases.

4. A new tool for flame images postprocessing

To directly determine the burning velocity using the Eq. (1), two quantities must be known: the flame propagation speed and the fresh gas velocity at the entrance of the flame front. The major difficulty of this technique is in measuring the fresh gas velocity at the entrance of the preheat zone of the flame front. An accurate measurement of local fresh gas velocity must be obtained in a zone with a typical length of 1 mm. Therefore, the reliability of this measurement depends on the flame front detection (which must be achieved with subpixel accuracy) and on the capacity of the technique to determine the fresh gas velocity. To accomplish this, a new tool for tomographic image postprocessing has been developed, which will be presented in the following section.

4.1. Flame speed estimation

The laser tomography technique provides a visualization of the flame front propagation. The fresh gas mixture is seeded with silicon oil particles, which evaporate at the entrance of the flame front ($T_{\text{evaporation}}$ = 580 K). The flame surface is obtained by differentiation of the dark and bright areas on the flame images, representing burned and unburned states, respectively. To determine the flame speed, the contours of tomographic images, which are captured at several stages of flame development, are extracted using postprocessing functions. On each spherical flame image, a single contiguous region representing burned gases is isolated with subpixel resolution and its contour is then accurately detected using an algorithm based on the method of Suzuki and Abe [51]. The detected raw flame boundaries are smoothed by a lowpass filter to remove noise from the digitization steps and a least squares algorithm [52] calculates the circle best fit to the raw contour and the corresponding flame radius. The flame speed is then calculated from the temporal evolution of the flame front using Eq. (2).

4.2. Measurement of fresh gas velocity at the entrance of the flame front

Balusamy et al. [42] have recently presented an experimental approach to directly measure the fresh gas velocity from PIV images. The determination of the fresh gas velocity near the preheat zone of the flame front is solved by taking into account the local topology of the flame front. The PIV images are analyzed with an algorithm using an adaptive interrogation window scheme. Using this technique, the fresh gas velocity is measured locally at the entrance of the flame front. The aim of this present work is to complete the PIV approach of Balusamy et al. [42] by proposing a new algorithm that can take into consideration the overall topology of the flame front, assuming that the flame is homogeneous in the specific case of a laminar spherical expansion. This approach therefore enables us to determine a global value of the fresh gas velocity. This method is applied to flame front contours, which were extracted and filtered with the detection procedure described previously. For two successive tomographic images, the algorithm defines a region of interest (ROI), which fits the flame front contour as depicted in Fig. 2. In these experiments, the ROI is defined by the angle θ, which can be adjusted to fit the spherical flame in its entirety or not, and by its width, which is fixed at 5 mm (~100 pixels). As presented in Fig. 3, this ROI is then transformed into a Cartesian coordinate system using a bilinear interpolation scheme. An interrogation window with a typical width of 4 pixels (~0.2 mm) is located within this ROI defined by its length ($r \cdot \theta$). The width of the interrogation window has been minimized to reach the physical size of the particle image, which is close to 4 pixels. A wider interrogation window will decrease the spatial resolution of u_g and thinner interrogation will introduce more erroneous values of u_g. The interrogation window length can be adjusted to achieve the best correlation between both successive tomographic images. Once both interrogation windows are well defined, a matching method based on a two-dimensional normalized cross-correlation is used between windows of the two successive ROI. Two steps are necessary to determine the fresh gas velocity value at the entrance of the flame front based on the two successive tomographic images. The first stage consists of finding the best correlation between both interrogation windows by shifting only the second interrogation window in increments of one pixel in the direction normal to the flame front. With a fixed position of the first interrogation window, the evolution of the correlation peak intensity can be plotted against the shift of the second interrogation window. This correlogram is constructed with a maximum displacement of 80 pixels (~4 mm) along the normal to the flame front. The intensity of the correlation peak increases up to an optimum displacement (which is calculated using subpixel interpolation by a Gaussian five-points fit) and then decreases. This optimum displacement, which is designated by Δr_2^{opti} in Fig. 4, corresponds to a maximum correlation. We will use this value to calculate the fresh gas velocity ahead of the flame front.

To characterize the velocity profile ahead of the flame, the second stage of postprocessing consists of moving the first interrogation window pixel by pixel in the direction normal to the flame front. For each position (expressed by Δr_1) of this window, the first step of the template matching procedure is restarted. This procedure thereby associates each position (Δr_1) of the first interrogation window with an optimum displacement (Δr_2^{opti}) of the second interrogation window, corresponding to the best correlation for both particle images. The fresh gas velocity along the normal to the flame front, u_g^*, is then calculated using both these parameters in the relationship

$$u_g^* = \frac{r_2 - r_2}{\Delta t} + \frac{\Delta r_2^{opti} - \Delta r_2}{\Delta t} = S + \frac{\Delta r_2^{opti} - \Delta r_2}{\Delta t}, \tag{10}$$

where r_1 and r_2 are radii of a flame image pair at time t and $t + \Delta t$ (Δt: time between two successive images), respectively, s is the flame speed, Δr_2^{opti} is the optimum displacement of the second interrogation window, and Δr_1 is the displacement of the first interrogation window. This relationship allows us to describe the movement of particles (i.e. fresh gases) pushed by the flame front expansion. Using this procedure, the fresh gas velocity profile along the normal to the flame front can be recorded from a distance of 150 μm (~3 pixels) up to 4 mm (~80 pixels). An example of an instantaneous fresh gas velocity profile calculated from methane/air flame images is presented in Fig. 5. In the case of spherically expanding flames, heat diffusion in the preheat zone influences the fresh gas velocity, u_g^*, which has a maximal value at the entrance of the flame front (expressed by u_g) and then decreases ahead of the flame front. This decrease occurs due to temperature and gas density variations through the flame front (Groot and De Goey [53]). In Fig. 5, the maximum fresh gas velocity, u_g, is obtained by fitting the velocity profile by a 10th order polynomial fit. For a particle image couple, postpro-

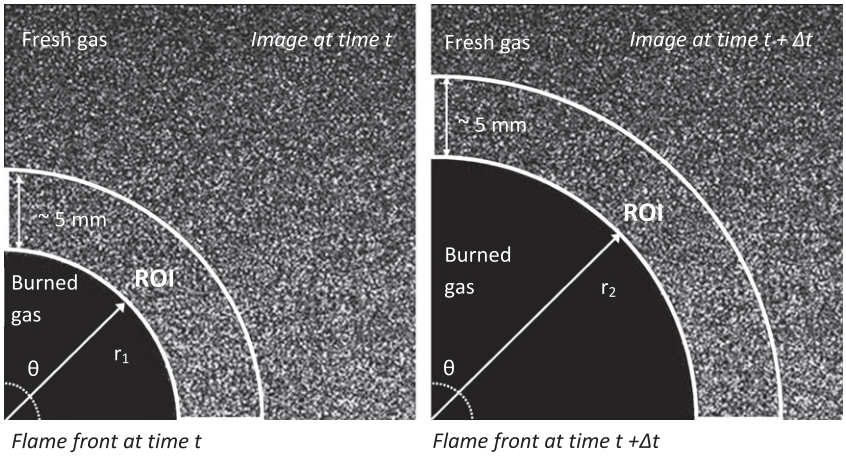

Fig. 2. Localization (in polar coordinates) of the region of interest (ROI) for a tomographic image couple.

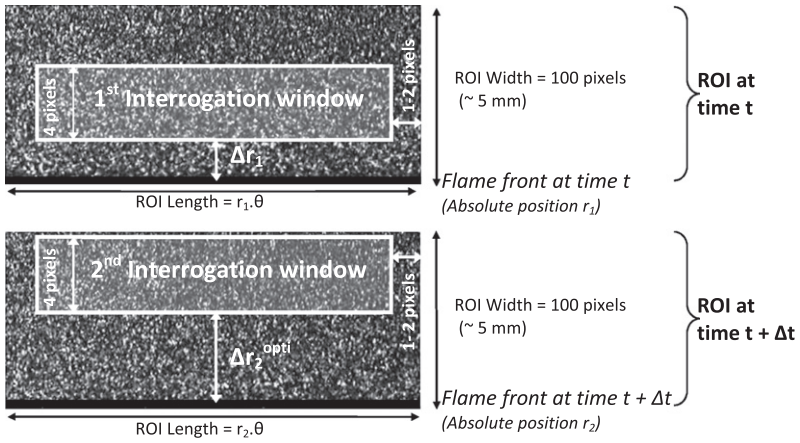

Fig. 3. Localization and displacement of both interrogation windows within the ROI (expressed in Cartesian coordinates) to find the maximum correlation.

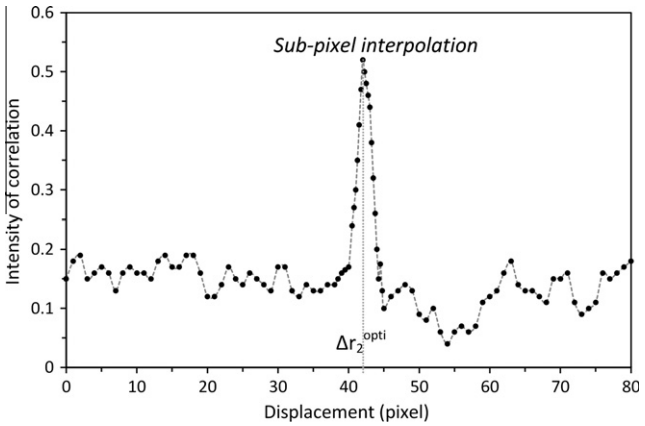

Fig. 4. Evolution of the correlation peak intensity as a function of the displacement between the two interrogation windows.

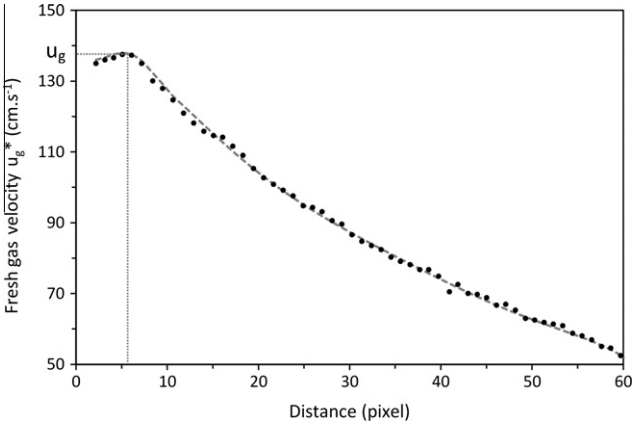

Fig. 5. Profile of the normal component of fresh gas velocity (10th order polynomial fit) calculated from two successive tomographic images; time of flame propagation after ignition: 5.8 ms (CH_4/air mixture, $\Phi = 1$, $P = 0.24$ MPa, $T = 298$ K).

cessed with the new algorithm, the maximum of the fresh gas velocity profile (u_g) is located around 7–8 pixels (~350–400 μm) ahead of the evaporation isotherm of the particles. For each image pair, the maximal value of the fresh gas velocity (u_g) at the entrance of the flame front is calculated and the laminar burning velocity is extracted using Eq. (1). The laminar burning velocity is then plotted as a function of the flame stretch rate; the unstretched burning velocity and the Markstein length relative to fresh gases are extrapolated from nonlinear or linear formulations (cf. Eqs. (4) and (5)).

5. Experimental results

Three fuels are investigated in this work: methane, isooctane, and ethanol (cf. Table 1).

The new postprocessing procedure is applied to flame images to extract the laminar flame speed and the fresh gas velocity at the entrance of the flame front. The unstretched laminar burning velocity is then determined using both approaches described in Section 3. First, the new postprocessing procedure is applied to methane/air flames for which values of unstretched laminar burning velocity are well known in the literature. Values of burned gas Markstein length are reported and compared with data from the literature. Second, new values of Markstein length relative to fresh gases are presented. To conclude, isooctane and ethanol/air mixtures are studied using this new procedure.

5.1. Methane/air flames

5.1.1. Laminar flame speed measurements – comparison with literature

Laminar flame speed measurements of methane/air flames are carried out for various equivalence ratios at atmospheric pressure and room temperature (298 K). For each test, around 80 images are taken covering the duration of flame propagation, free from ignition energy and wall effects. The unstretched flame speed is linearly and nonlinearly extrapolated. The nonlinear extraction of the unstretched flame speed, which is used in this work, is derived from the methodology of Halter et al. [46] based on a minimization of the expression (6).

In order to validate the accuracy of our experimental measurements, a comparison with results from the literature is carried out and is presented in Fig. 6. The unstretched laminar burning velocity values are deduced from the laminar flame speed using Eq. (9). This figure compares our experimental values for the unstretched laminar burning velocity with other recent data [3,4,6,8–10,12–14,25,54] (which are acquired by employing a combustion vessel and are determined by linear extrapolation to a zero strain rate) and numerical results using GRI-Mech 3.0 [55] and GRI-Mech 2.11 [56]. For an equivalence ratio range of 0.6–1.3, experimental data of the present work are in good agreement with those of other studies, especially with results of Tahtouh et al. [54]. A good agreement with numerical results is also found, particularly using the mechanism GRI-Mech 3.0. This agreement suggests the accuracy of the algorithm used for the flame front extraction and the flame speed calculation. Fig. 7 illustrates the influence of linear and nonlinear extrapolation of the unstretched flame speed on the unstretched burning velocity. The two methods provide similar results in the case of lean and stoichiometric methane/air mixtures, but for rich mixtures some differences appear. In fact, according to the results of Tahtouh et al. [45] and Halter et al. [46], the nonlinear method is more suitable to extract the unstretched flame speed in the case of rich methane/air mixtures.

To illustrate the influence of linear and nonlinear extrapolation on the unstretched flame speed, the evolution of flame speed as a function of flame stretch is presented in Figs. 8 and 9 for two different equivalence ratios, 1 and 1.2, respectively. As shown in these figures, the linear approximation is no longer valid for equivalence ratios higher than 1 and overestimates the unstretched flame speed and thus the unstretched burning velocity. The assumption $s/s^0 \approx 1$, which allows the formulation (7), is not satiesfied and therefore the nonlinear extrapolation must be used. Hereafter, all experimental data in this study will be nonlinearly extracted.

5.1.2. Fresh gas velocity and Markstein length measurements

The main advantage of the new postprocessing procedure is its ability to determine a global value of the fresh gas velocity, u_g, at the entrance of the flame front. This procedure is now applied to methane/air flame images for various equivalence ratios at 0.1 MPa and 298 K. Variations of the fresh gas velocity and flame

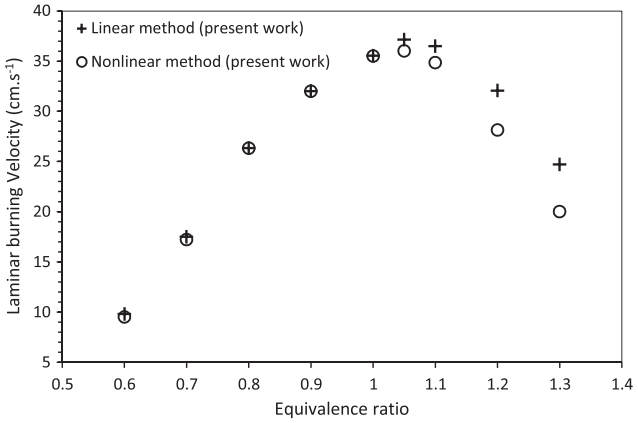

Fig. 7. Relationship between unstretched laminar burning velocity ($u_s^0 = (\rho_b/\rho_u) \cdot s^0$) and equivalence ratio (CH_4/air mixture, $P = 0.1$ MPa, $T = 298$ K). Comparison of linear and nonlinear methodologies.

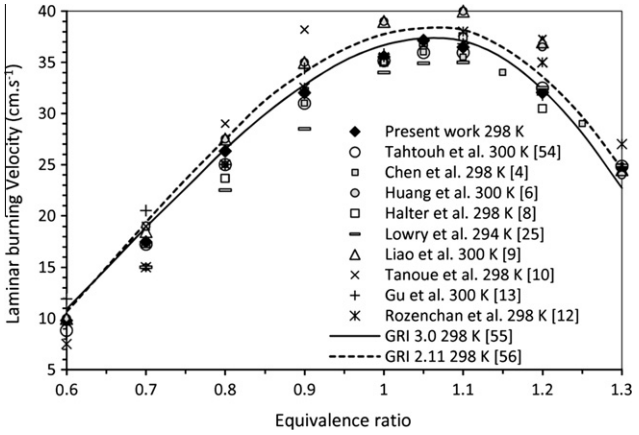

Fig. 6. Unstretched laminar burning velocity ($u_s^0 = (\rho_b/\rho_u)s^0$) (linearly extracted) plotted against equivalence ratio. (CH_4/air mixture, $P = 0.1$ MPa, $T = 298$ K). Comparison with experimental data of previous works and calculations with GRI-MECH 3.0 and GRI-MECH 2.11.

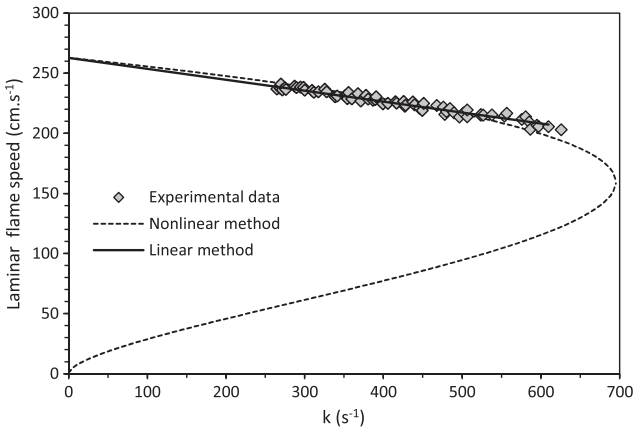

Fig. 8. Evolution of flame speed as a function of flame stretch. Comparison of linear and nonlinear extrapolations of experimental data (CH_4/air mixture, $\Phi = 1$, $P = 0.1$ MPa, $T = 298$ K).

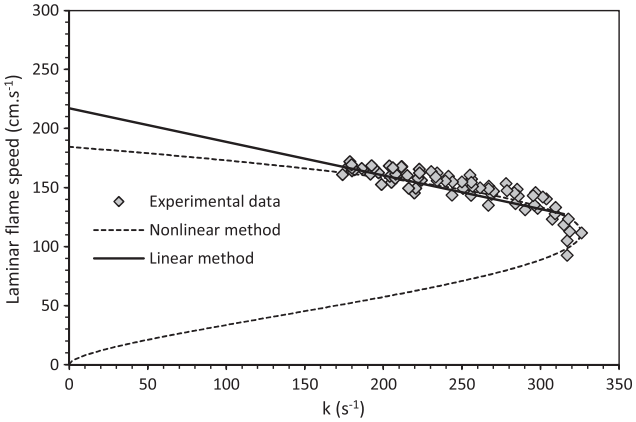

Fig. 9. Evolution of flame speed as a function of flame stretch. Comparison of linear and nonlinear extrapolations of experimental data (CH_4/air mixture, $\Phi = 1.2$, $P = 0.1$ MPa, $T = 298$ K).

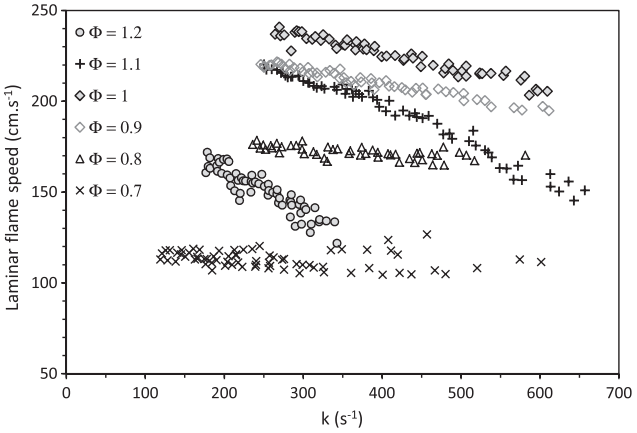

Fig. 11. Variation of laminar flame speed, s, as a function of flame stretch. (CH_4/air mixture, $P = 0.1$ MPa, $T = 298$ K).

speed as a function of the stretch rate are shown in Figs. 10 and 11, respectively. In order to show the reproducibility of each experiment, data of five consecutive measurements are regrouped in these figures. For all investigated mixtures, decreasing the stretch rate accelerates fresh gases and flame front. As in the relationship between flame speed and stretch rate, linear and nonlinear variations of the fresh gas velocity versus the flame stretch can be expected. Moreover, the equivalence ratio has the same influence on the evolution of fresh gas velocity and flame speed versus the stretch. The burning velocity is then directly calculated using the difference between values of fresh gas velocity and flame speed (cf. Eq. (1)). In Fig. 12, the laminar burning velocity and the flame speed divided by the ratio of the densities of unburned to adiabatically burned gas are plotted as a function of flame stretch for a stoichiometric methane/air mixture at 0.1 MPa and 298 K. In this graph, the two expressions ($u_n = s - u_g$ and $(\rho_b/\rho_u)\cdot s$) present two very different evolutions versus the stretch, but in the case of methane/air flames they give nearly the same laminar burning velocity as when they are extrapolated to a zero stretch rate: $u_n^0 = 35.5 \pm 0.5$ cm s^{-1}. As detailed in the computational study of Bradley et al. [40], the relation $((\rho_b/\rho_u)\cdot s)$ assumes zero flame thickness and it does not describe the sensitivity of the burning rate to the flame stretch. This relation is only valid to determine the unstretched laminar burning velocity when the flame radius tends to infinity:

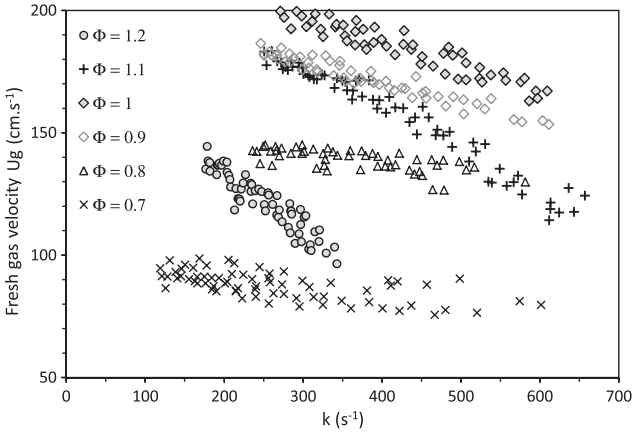

Fig. 10. Variation of fresh gas velocity, u_g, as a function of flame stretch. (CH_4/air mixture, $P = 0.1$ MPa, $T = 298$ K).

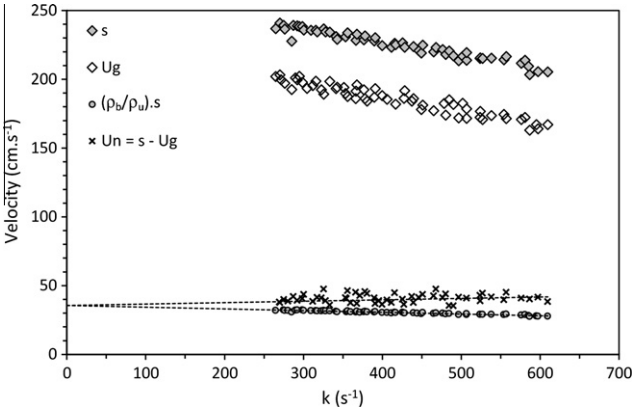

Fig. 12. Variation of flame speed, fresh gas velocity and burning velocity as a function of flame stretch. Comparison between the two procedures of burning velocity calculation (CH_4/air mixture, $\Phi = 1$, $P = 0.1$ MPa, $T = 298$ K).

$$u_n^0 \cong u_s^0 = lim_{r\to\infty}\left(\frac{\rho_b}{\rho_u}\cdot S\right) = \frac{\rho_b}{\rho_u}\cdot S^0 \qquad (11)$$

The direct determination of the burning velocity based on flame speed and fresh gas velocity measurements enables us to characterize the relationship between the burning rate and the flame stretch and to accurately determine the unstretched laminar burning velocity without the use of fuel properties:

$$u_n^0 = \lim_{r\to\infty}(S - u_g). \qquad (12)$$

Flame response in terms of flame speed and burning velocity to flame stretch is quantified by the burned gas Markstein length, L_b, and the unburned gas Markstein length, L_u, respectively. Thanks to the new postprocessing procedure, this is the first time (to our knowledge) that experimental values of L_u have been presented in the literature for spherical laminar methane/air flames. The values of L_u and L_b are deduced using linear and nonlinear formulations and they are summarized in Table 2 for an equivalence ratio range of 0.7–1.2. For all the mixtures investigated, the flame speed increases when the stretch rate decreases; therefore all the values of burned gas Markstein length, L_b, are positive. In Fig. 13, values of burned gas Markstein length, which are deduced from the linear relation, are compared to data found in the literature [13,40,46]. The burned gas Markstein length increases when the equivalence ratio increases. This evolution is consistent with all previous results, but in our case the influence of the equivalence ratio on the flame sensitivity to stretch is much more accentuated. In Fig. 14, values

Table 2
Values of burned gas Markstein length L_b and unburned gas Markstein length L_u. Comparison of linear and nonlinear methodologies (CH_4/air mixture, T = 298 K, P = 0.1 MPa).

Φ	L_b (mm) linear method	L_b (mm) nonlinear method	L_u (mm) linear method	L_u (mm) nonlinear method
0.7	0.16	0.11	−0.31	−0.35
0.8	0.40	0.40	−0.20	−0.22
0.9	0.59	0.52	−0.19	−0.20
1	0.90	0.70	−0.11	−0.13
1.1	1.7	0.73	0.10	0.04
1.2	2.7	1.1	0.25	0.13

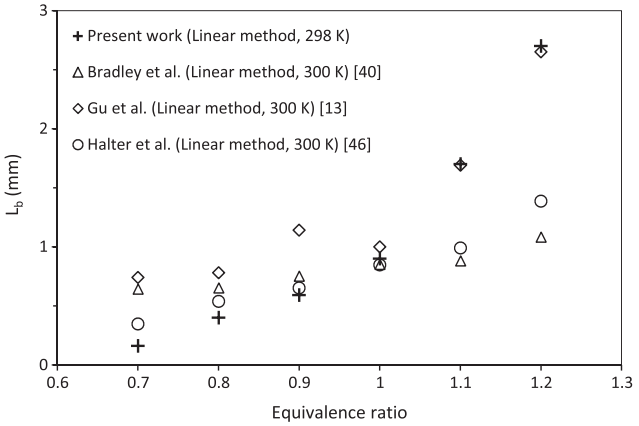

Fig. 13. Burned gas Markstein lengths for methane/air mixture (P = 298 K, T = 0.1 MPa).

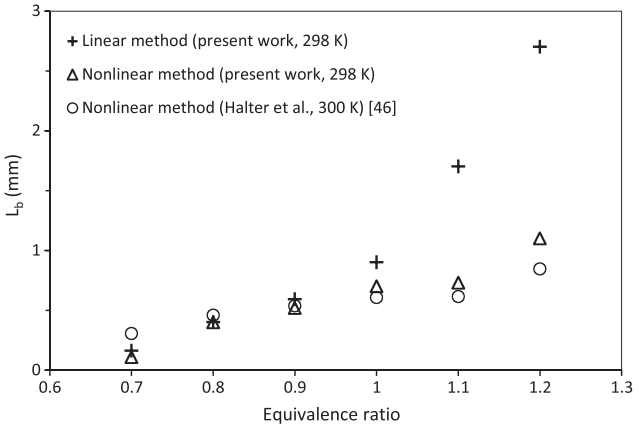

Fig. 14. Burned gas Markstein lengths for methane/air mixture. Comparison of linear and nonlinear methodologies (P = 298 K, T = 0.1 MPa).

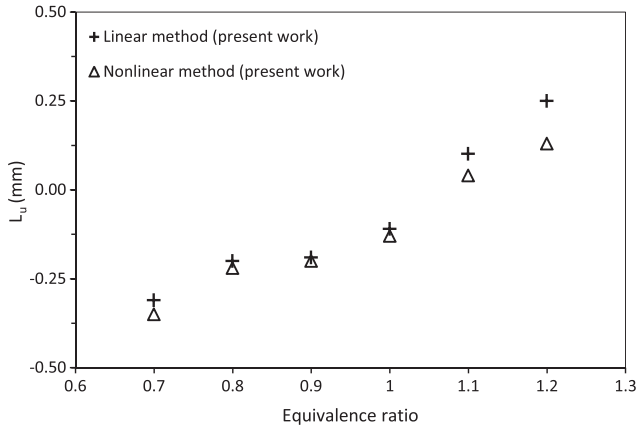

Fig. 15. Unburned gas Markstein lengths for methane/air mixture. Comparison of linear and nonlinear methodologies (P = 298 K, T = 0.1 MPa).

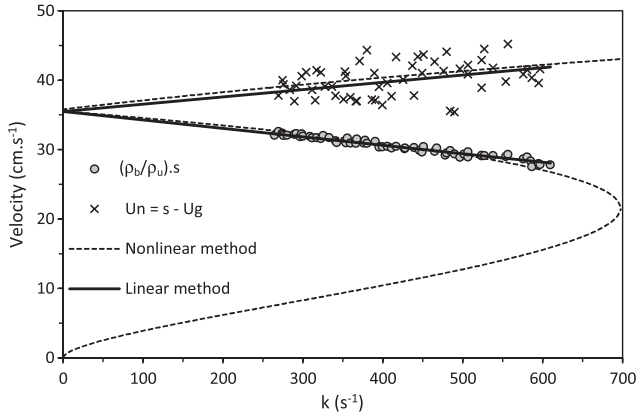

Fig. 16. Linear and nonlinear relationships between laminar burning velocity and flame stretch. Comparison between the two procedures of burning velocity calculation (CH_4/air mixture, Φ = 1, P = 0.1 MPa, T = 298 K).

of burned gas Markstein length are deduced from the nonlinear relation and they are in very good agreement with the data of Halter et al. [46]. Comparison between linear and nonlinear methods shows that for rich mixtures the burned gas Markstein length evaluated with the linear formulation is overestimated and therefore, as presented in the previous section, the corresponding flame speed is overstated as well.

In Table 2, the unburned gas Markstein length, L_u, is negative for an equivalence ratio range of 0.7–1 and changes sign for equivalence ratios higher than 1. The negative value of the unburned gas Markstein length, L_u, indicates that the burning rate decreases when of the flame stretch decreases (i.e., when the flame radius tends to infinity). The evolution of the unburned gas Markstein length as a function of the equivalence ratio is plotted in Fig. 15. Increasing the equivalence ratio increases L_u. The use of a linear method is valid up to an equivalence ratio of 1, but for richer mixtures linear values of L_u are two times those obtained with the nonlinear method. This overestimation in L_u will result in an overestimation of the unstretched laminar burning velocity. This observation is illustrated in Figs. 16 and 17, in which linear and nonlinear extrapolations of the unstretched burning velocity are plotted and compared for the case of stoichiometric and rich methane/air mixtures. In Fig. 16, for an equivalence ratio of 1, linear and nonlinear values of unstretched burning velocity are similar. Additionally, this observation is verified for both approaches of the unstretched burning velocity calculation (cf. Eqs. (11) and (12)). In Fig. 17, for an equivalence ratio of 1.2, some substantial differences appear at a zero stretch rate between linear and nonlinear formulations of burning velocity and overestimation by 12% is observed

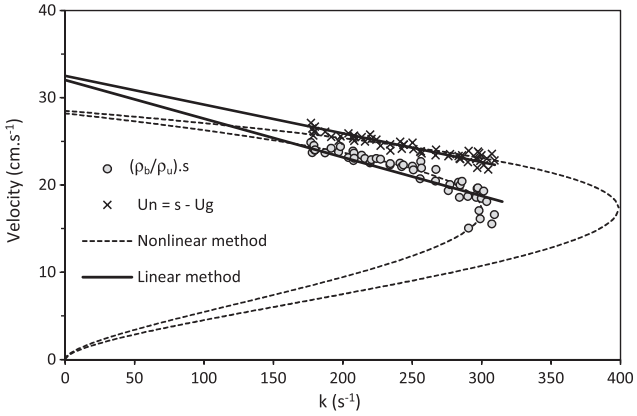

Fig. 17. Linear and nonlinear relationships between laminar burning velocity and flame stretch. Comparison between the two procedures of burning velocity calculation (CH_4/air mixture, $\Phi = 1.2$, $P = 0.1$ MPa, $T = 298$ K).

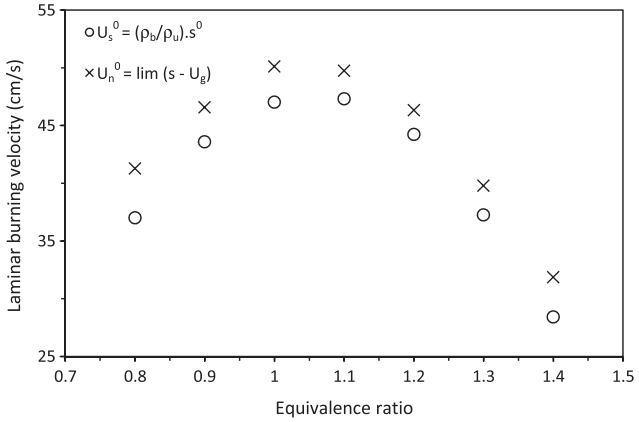

Fig. 19. Unstretched laminar burning velocity (nonlinearly extracted) plotted against equivalence ratio. Comparison between the two approaches of unstretched burning velocity calculation (C_8H_{18}/air mixture, $P = 0.1$ MPa, $T = 373$ K).

in the case of the linear extrapolation. Therefore, the nonlinear determination must be systematically applied in order to obtain more accurate values of the unstretched burning velocity. In the following sections of this study, describing our experimental results of isooctane and ethanol/air mixtures, all data will be exclusively nonlinearly extrapolated.

To conclude, Fig. 18 compares nonlinear values of the unstretched laminar burning velocity that were extracted using both processing approaches for an equivalence ratio range of 0.7–1.2. In the case of a methane/air mixture, both approaches provide similar results, which suggests the new postprocessing procedure's accuracy in extracting the fresh gas velocity at the entrance of the flame front as well as attesting to the validity of assumptions used to calculate the burned gas density.

5.2. Isooctane/air flames

First, in the case of isooctane/air mixtures, nonlinear values of the unstretched laminar burning velocity (u_s^0) (extracted using Eq. (11)) are plotted against the equivalence ratio in Fig. 19 for the following experimental conditions: 373 K, 0.1 MPa. The isooctane burning velocity exhibits a slight shift toward the fuel-rich region similar to the behavior of methane/air flames, where the maximal burning velocity peaks at 1.05. This trend is the same as those observed in previous studies [46,57], whose values of burning velocity were also nonlinearly extracted. A comparison between the two approaches to the unstretched burning velocity calculation is also presented in this Figure. The equivalence ratio's influence on the unstretched burning velocity is the same for both approaches but values of the unstretched burning velocity obtained directly using Eq. (12) are 5–12% higher than those calculated using Eq. (11). Therefore, in the case of isooctane/air mixtures, the formulation (11) underestimates the unstretched laminar burning velocity and involves inaccurate results because u_s^0 differs from u_n^0. Recently, this difference has also been pointed out by Balusamy et al. [42] for propane/air mixtures at various equivalence ratios, in which case the underestimation of u_s^0 is due to confinement effects of the wall, which tend to reduce the flame speed for the larger flame radius. In our study, this explanation does not apply to methane/air flames, in which there is no difference between u_s^0 and u_n^0. We therefore conclude that the principal reason for this difference in the case of isooctane/air flames lies in the burned gas density calculation that is used to determine the value of u_s^0. We will present some explications of this difference in the next section for ethanol/air flames where similar results are observed also.

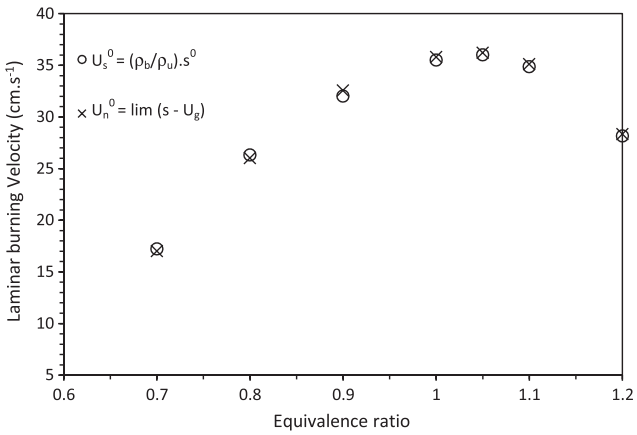

Fig. 18. Unstretched laminar burning velocity (nonlinearly extracted) plotted against equivalence ratio. Comparison between the two approaches of unstretched burning velocity calculation (CH_4/air mixture, $P = 0.1$ MPa, $T = 298$ K).

Nonlinear values of L_u and L_b are also determined by the new approach; they are summarized in Table 3 and are plotted against the equivalence ratio in Fig. 20. The decrease of L_u and L_b with Φ is associated with a decreasing Lewis number. This is an evolution opposite to that previously observed in the case of methane/air mixtures, whose Lewis number increases with Φ. Our experimental values of burned gas Markstein length, L_b, are in good agreement with data of Halter et al. [46]. For an equivalence ratio range of 0.8–1.3, the values of L_b are positive and change sign for higher equivalence ratios corresponding to a decrease of the flame speed when the flame radius tends to infinity. Concerning the unburned gas Markstein length, all the values of L_u are negative for

Table 3
Values of burned gas Markstein length L_b and unburned gas Markstein length L_u. (C_8H_{18}/air mixture, $P = 0.1$ MPa, $T = 373$ K).

Φ	L_b (mm) nonlinear method	L_u (mm) nonlinear method
0.8	1.1	0.04
0.9	0.89	−0.07
1	0.74	−0.09
1.1	0.60	−0.20
1.2	0.40	−0.26
1.3	0.08	−0.36
1.4	−0.63	−0.50

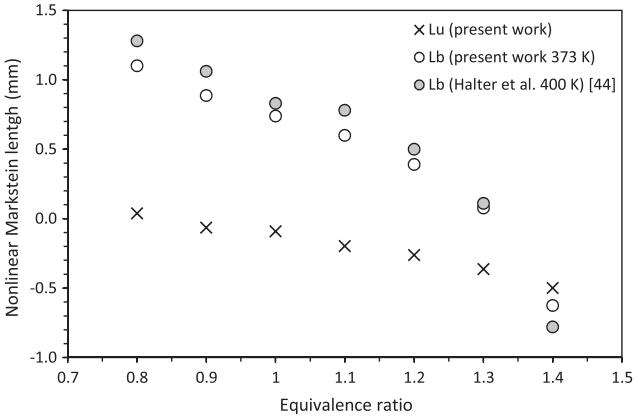

Fig. 20. Nonlinear values of burned and unburned gas Markstein lengths for isooctane/air mixture. (P = 0.1 MPa, T = 373 K). Comparison with previous work.

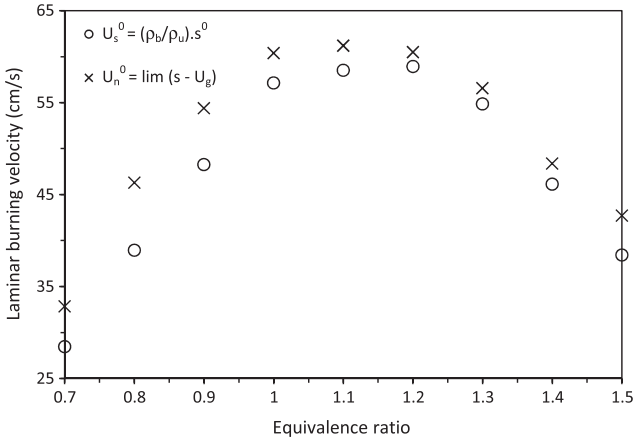

Fig. 22. Unstretched laminar burning velocity (nonlinearly extracted) plotted against equivalence ratio. Comparison between the two approaches of unstretched burning velocity calculation (C_2H_5OH/air mixture, P = 0.1 MPa, T = 373 K).

equivalence ratios higher than 0.8, indicating that the burning velocity decreases when the flame stretch decreases.

5.3. Ethanol/air flames

In Fig. 21, nonlinear values of the unstretched laminar burning velocity (u_s^0) are plotted against the equivalence ratio and compared to data of Broustail et al. [57]. Because of the temperature difference between the two experiments, unstretched laminar burning velocities of Broustail et al. [57] are higher than the data of our study, but they present the same trend against the equivalence ratio and the maximum velocity is close to Φ = 1.1. The two approaches to unstretched burning velocity calculations are compared in Fig. 22, and they have different magnitudes, particularly at equivalence ratios lower than 1. In this pressure range, values of u_s^0 are 13–19% lower than values of u_n^0. This difference decreases by 2.5–6% for richer mixtures. As in the previous case of isooctane/air mixtures, the formulation (11) underestimates the unstretched laminar burning velocity for ethanol/air flames.

The main reason of this difference comes from the burned gas density estimation (generally computed for burned gases at chemical equilibrium for an adiabatic combustion) in Eq. (9). So, if differences are observable between these two methods, it means either that the experimental flame is subjected to radiative effects (emission and absorption) or that the burned gases have not reached a chemical equilibrium state, for the propagation times investigated in the experiments.

The first effect concerns radiative emission and absorption, which are not taken into account in the adiabatic and equilibrium temperature. In the literature [48], this effect was numerically studied when the mixture was diluted by vapor or by CO_2. It was found that reabsorption of emitted radiation led to substantially higher burning velocities, particularly when CO_2, a strong absorber, was present in the unburned gas. For our experimental conditions, the IR spectra of isooctane and ethanol do not present any absorption in the wavelengths of CO_2 and H_2O emissions. In this way, radiative effects would not be the dominant effect of this difference.

The second point could be linked to the equilibrium state of the burned gases in the experiments. Indeed, due to the finite size of the flame kernels (maximum radius 2 cm), it may possible that the time or the distance to reach the equilibrium state cannot be obtained in the experimental configuration. To evaluate this effect, we use a kinetic modeling using the COSILAB package. The premixed flame is modeled by a "freely propagating flame" code, with GRI 3.0 kinetic mechanism for methane and a Konnov (release 0.5) mechanism for ethanol.

For atmospheric conditions, the temperature profiles normalized by equilibrium temperature across the flame front are reported in Fig. 23. For methane/air flames, the distance to reach equilibrium is less than 1 cm, which corresponds to a typical flame radius at a small propagation time. This also has been observed by Bradley [40], who has computed the temporal evolution of the

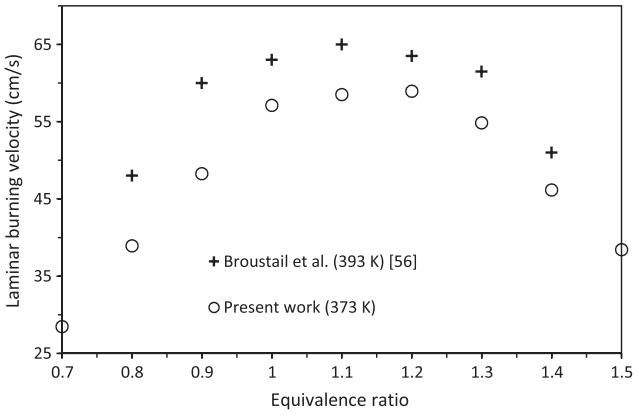

Fig. 21. Unstretched laminar burning velocity ($u_s^0 = (\rho_b/\rho_u) \cdot s^0$) (nonlinearly extracted) plotted against equivalence ratio. Comparison with previous work (C_2H_5OH/air mixture, P = 0.1 MPa).

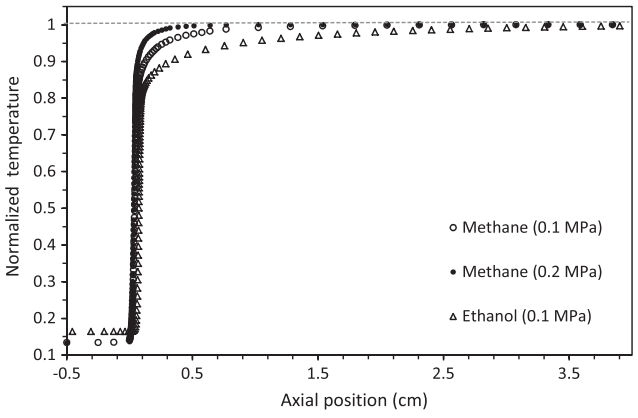

Fig. 23. Temperature profiles for stoichiometric mixtures of methane and ethanol. (For each case, the temperature is normalized by the equilibrium temperature of burned gases).

flame temperature of freely propagating flames. One can observe that the temperature profiles according to time show the reaction to take some time (few ms) to be completed and to reach chemical equilibrium. At the end of propagation (i.e., for large flame radius), the temperature profiles in the burned gases are globally flat and equal to the equilibrium temperature. In this way, for the measurements (methane/air flames), both methods give globally the same results.

For ethanol and isooctane ($P = 0.1$ MPa), the differences are larger. In Fig. 23, it clearly appears that the distance to reach the equilibrium state in the burned gases is higher than for the methane/air flames and also larger than for the typical flame of the experiments at the end of the propagation time. An equilibrium solver for the density ratio could produce some error for these conditions, because it artificially decreases the density ratio and then decreases the unstretched burning velocity.

The pressure effect on the laminar burning velocity is then studied for a stoichiometric ethanol/air mixture at 373 K in Fig 24. The pressure influence is characteristic of hydrocarbon/air mixtures and increasing the pressure from 0.1 to 0.5 MPa decreases the burning velocity by 33%. For this pressure range, no cellular structure appears during the flame front propagation.

It is worth noting also that for high pressure conditions, the difference between the two methods decreases and becomes negligible at 0.4 MPa (Fig. 24). This can be explained by the Figs. 23 and 25, where it clearly appears that the equilibrium state of the burned gases is obtained faster when the pressure increases.

In this way, the method proposed in this paper does not require any assumption of adiabaticity or full equilibrium state of the burned gases to experimentally determine the unstretched laminar burning velocity.

Nonlinear values of L_u and L_b are presented in Table 4 and they are plotted against equivalence ratios at 0.1 MPa and 373 K in Fig. 26. As for the isooctane/air mixture, increasing the equivalence ratio decreases Markstein lengths, L_u and L_b. This trend agrees well with results of Broustail et al. [57] and it can also be associated with a decreasing Lewis number with Φ. For the ethanol/air mixture, all values of L_b are positive and values of L_u are negative for equivalence ratios higher than 0.8.

Table 4
Values of burned gas Markstein length L_b and unburned gas Markstein length L_u. (C_2H_5OH/air mixture, $P = 0.1$ MPa, $T = 373$ K).

Φ	L_b (mm) nonlinear method	L_u (mm) nonlinear method
0.7	1.14	0.07
0.8	0.89	0.06
0.9	0.66	−0.04
1	0.77	−0.15
1.1	0.66	−0.16
1.2	0.62	−0.18
1.3	0.46	−0.22
1.4	0.27	−0.24
1.5	0.04	−0.26

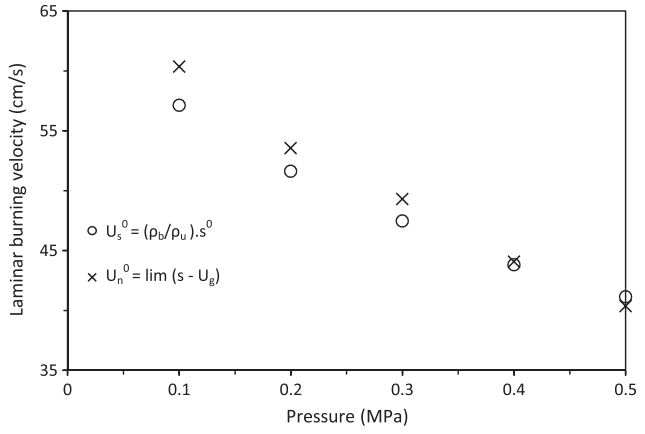

Fig. 24. Unstretched laminar burning velocity (nonlinearly extracted) plotted against pressure. Comparison between the two approaches of unstretched burning velocity calculation (C_2H_5OH/air mixture, $\Phi = 1$, $T = 373$ K).

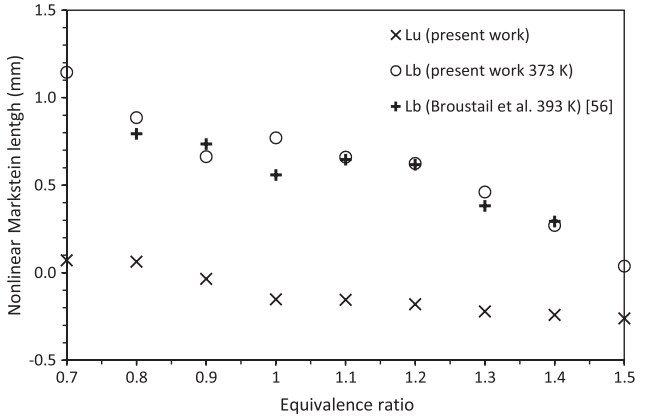

Fig. 26. Nonlinear values of burned and unburned gas Markstein lengths for ethanol/air mixtures. ($P = 0.1$ MPa, $T = 373$ K). Comparison with previous work.

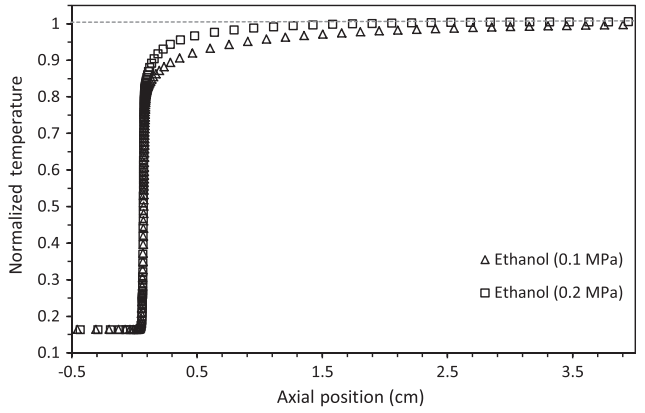

Fig. 25. Temperature profiles for stoichiometric mixture of ethanol. For each case, the temperature is normalized by the equilibrium temperature of burned gases.

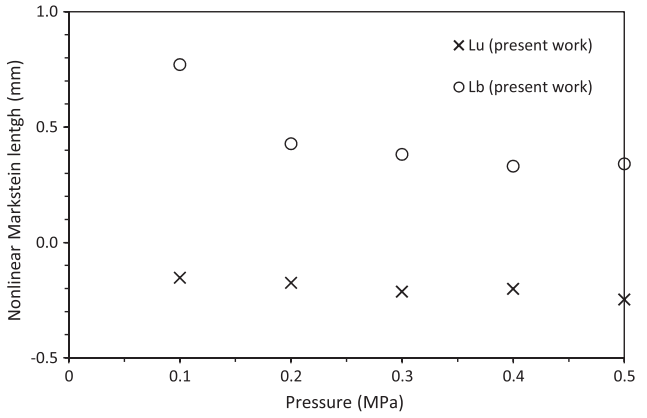

Fig. 27. Nonlinear values of burned and unburned gas Markstein lengths plotted against pressure. (C_2H_5OH/air mixture, $\Phi = 1$, $T = 373$ K).

Table 5
Values of burned gas Markstein length L_b and unburned gas Markstein length L_u. (C_2H_5OH/air mixture, $\Phi = 1$, $T = 373$ K).

P (MPa)	L_b (mm) nonlinear method	L_u (mm) nonlinear method
0.1	0.77	−0.15
0.2	0.43	−0.18
0.3	0.38	−0.21
0.4	0.33	−0.20
0.5	0.34	−0.25

Nonlinear values of L_u and L_b are also plotted against pressure (Fig. 27) and detailed in Table 5. The pressure effect is most significant from 0.1 to 0.2 MPa and strongly influences values of L_b, which decreases by 44% in this pressure range. L_u is less affected by the pressure influence.

6. Conclusion

A new tool for extracting the laminar burning velocity has been detailed and validated in the case of spherically outwardly expanding flames. This postprocessing procedure directly determines the laminar burning velocity from the flame speed and the global fresh gas velocity near the preheat zone of the flame front; furthermore, it characterizes the influence of external flame stretching on the burning velocity by measuring the Markstein length for the unburned gases, L_u. Thus, this direct approach gives more information in terms of burning rate sensitivity to flame stretch and more accurate measurements than the standard approach that is commonly used in the literature and that requires knowledge of the fuel mixture properties.

In this work, methane, isooctane, and ethanol/air flames have been studied under various experimental conditions ($0.6 \leqslant \Phi \leqslant 1.5$, $298 \leqslant T \leqslant 373$ K, $0.1 \leqslant P \leqslant 0.5$ MPa). The influence of linear and nonlinear extrapolation on the unstretched burning velocity has been tested and, as previously presented in the literature, linear extrapolation results in overestimation of the unstretched burning velocity. Next, the unstretched laminar burning velocity has been nonlinearly extracted using the two processing approaches and results have been compared. In the case of methane/air mixtures, the two methods give nearly the same results, but some differences appear for isooctane and ethanol/air mixtures.

The main reason for the difference between the two methods comes from the burned gas density estimation (computed for burned gases at chemical equilibrium for adiabatic combustion). In the case of the isooctane and ethanol/air mixture, the burned gases have not reached a chemical equilibrium state for the propagation times investigated in the experiments. Indeed, due to the finite size of the flame kernels (maximum radius 2 cm), the time or the distance to reach the equilibrium state cannot be obtained in the experimental configuration for these mixtures.

So an equilibrium solver for the density ratio could produce some error for these conditions because it artificially decreases the density ratio and thus decreases the unstretched burning velocity.

Values of L_u, which represents the sensitivity of the burning rate to the flame stretch, have been determined and two opposite evolutions have been observed, depending on the equivalence ratio: for methane, L_u increases with Φ and for isooctane and ethanol, L_u decreases with Φ. These evolutions can be correlated with the Lewis number of the respective mixtures.

Acknowledgments

This material is based on work supported by the European Regional Development Fund under Grant Interreg IV C5. We thank Dr. G. Godard and Dr. F. Corbin for their assistance in software development.

References

[1] W.-D. Hsieh, R.-H. Chen, T.-L. Wu, T.-H. Lin, Atmos. Environ. 36 (3) (2002) 403–410, doi:10.1016/s1352-2310(01)00508-8.
[2] S.H. Park, I.M. Youn, C.S. Lee, Fuel 90 (2) (2011) 748–755, doi:10.1016/j.fuel.2010.08.029.
[3] X. Qin, Y. Ju, Proc. Combust. Inst. 30 (1) (2005) 233–240.
[4] Z. Chen, X. Qin, Y. Ju, Z. Zhao, M. Chaos, F.L. Dryer, Proc. Combust. Inst. 31 (1) (2007) 1215–1222.
[5] M.P. Burke, Z. Chen, Y. Ju, F.L. Dryer, Combust. Flame 156 (4) (2009) 771–779.
[6] Z. Huang, Y. Zhang, K. Zeng, B. Liu, Q. Wang, D. Jiang, Combust. Flame 146 (1-2) (2006) 302–311.
[7] M. Ilbas, A.P. Crayford, I. Yilmaz, P.J. Bowen, N. Syred, Int. J. Hydrogen Energy 31 (12) (2006) 1768–1779.
[8] F. Halter, C. Chauveau, N. Djebaili-Chaumeix, I. Gokalp, Proc. Combust. Inst. (2005) 201–208.
[9] S.Y. Liao, D.M. Jiang, J. Gao, Z.H. Huang, Energy Fuels 18 (2) (2004) 316–326.
[10] K. Tanoue, F. Shimada, T. Hamatake, JSME Int. J., Ser. B: Fluids Therm. Eng. 46 (3) (2003) 416–424.
[11] C. Mandilas, M.P. Ormsby, C.G.W. Sheppard, R. Woolley, Proc. Combust. Inst. 31 (1) (2007) 1443–1450.
[12] G. Rozenchan, D.L. Zhu, C.K. Law, S.D. Tse, Proc. Combust. Inst. 29 (2) (2002) 1461–1470.
[13] X.J. Gu, M.Z. Haq, M. Lawes, R. Woolley, Combust. Flame 121 (1-2) (2000) 41–58.
[14] M.I. Hassan, K.T. Aung, G.M. Faeth, Combust. Flame 115 (4) (1998) 539–550.
[15] K.T. Aung, L.K. Tseng, M.A. Ismail, G.M. Faeth, Combust. Flame 102 (4) (1995) 526.
[16] S.C. Taylor, D.B. Smith, Combust. Flame 102 (4) (1995) 523–525.
[17] R. Stone, A. Clarke, P. Beckwith, Combust. Flame 114 (3-4) (1998) 546–555.
[18] D. Bradley, R.A. Hicks, M. Lawes, C.G.W. Sheppard, R. Woolley, Combust. Flame 115 (1-2) (1998) 126–144.
[19] S. Jerzembeck, N. Peters, P. Pepiot-Desjardins, H. Pitsch, Combust. Flame 156 (2) (2009) 292–301.
[20] D. Bradley, M. Lawes, M.S. Mansour, Combust. Flame 156 (Compendex) (2009) 1462–1470.
[21] K. Eisazadeh-Far, A. Moghaddas, J. Al-Mulki, H. Metghalchi, Proc. Combust. Inst. 33 (1) (2011) 1021–1027, doi:10.1016/j.proci.2010.05.105.
[22] A.A. Konnov, R.J. Meuwissen, L.P.H. de Goey, Proc. Combust. Inst. 33 (1) (2011) 1011–1019, doi:10.1016/j.proci.2010.06.143.
[23] S.Y. Liao, D.M. Jiang, Z.H. Huang, K. Zeng, Q. Cheng, Appl. Therm. Eng. 27 (2-3) (2007) 374–380, doi:10.1016/j.applthermaleng.2006.07.026.
[24] Ö.L. Gülder, Combust. Flame 56 (3) (1984) 261–268, doi:10.1016/0010-2180.84)90060-9.
[25] W. Lowry, J. de Vries, M. Krejci, E. Petersen, Z. Serinyel, W. Metcalfe, H. Curran, G. Bourque, J. Eng. Gas Turbines Power 133 (9) (2011). 091501-9 10.1115/1.4002809.
[26] Y. Dong, C.M. Vagelopoulos, G.R. Spedding, F.N. Egolfopoulos, Proc. Combust. Inst. (2002) 1419–1426.
[27] Y. Huang, C.J. Sung, J.A. Eng, Combust. Flame 139 (3) (2004) 239–251.
[28] C.M. Vagelopoulos, F.N. Egolfopoulos, Symp. (Int.) Combust. 27 (1) (1998) 513–519.
[29] C.M. Vagelopoulos, F.N. Egolfopoulos, C.K. Law, Symp. (Int.) Combust. 25 (1) (1994) 1341–1347.
[30] F.N. Egolfopoulos, P. Cho, C.K. Law, Combust. Flame 76 (3-4) (1989) 375–391.
[31] R.T.E. Hermanns, A.A. Konnov, R.J.M. Bastiaans, L.P.H. de Goey, K. Lucka, H. Kohne, Fuel 89 (1) (2010) 114–121.
[32] F.H.V. Coppens, A.A. Konnov, Fuel 87 (13–14) (2008) 2866–2870.
[33] F.H.V. Coppens, J. De Ruyck, A.A. Konnov, Combust. Flame 149 (4) (2007) 409–417.
[34] K.J. Bosschaart, L.P.H. De Goey, Combust. Flame 136 (3) (2004) 261–269.
[35] K.J. Bosschaart, L.P.H. De Goey, Combust. Flame 132 (1-2) (2003) 170–180.
[36] A. Van Maaren, D.S. Thung, L.R.H. De Goey, Combust. Sci. Technol. 96 (4) (1994) 327–344.
[37] B. Lewis, G. Von Elbe, Combustion, Flame and Explosions of Gases, third ed., Academic Press, Inc., New York, 1987.
[38] Y. Ogami, H. Kobayashi, JSME Int. J., Ser. B: Fluids Therm. Eng. 48 (3) (2006) 603–609.
[39] O. Kurata, S. Takahashi, Y. Uchiyama, SAE 942037 (1994).
[40] D. Bradley, P.H. Gaskell, X.J. Gu, Combust. Flame 104 (1-2) (1996) 176–198.
[41] B. Lecordier. Etude de l'interaction de la propagation d'une flamme de prémélange avec le champ aréodynamique par association de la tomographie laser et de la PIV. PhD Thesis Report, Université de Rouen, France, 1997.
[42] S. Balusamy, A. Cessou, B. Lecordier, Exp. Fluids, doi:10.1007/s00348-010-1027-5 (2010), doi:10.1007/s00348-010-1027-5.
[43] P. Clavin, Prog. Energy Combust. Sci. 11 (1) (1985) 1–59.
[44] A.P. Kelley, C.K. Law, Combust. Flame 156 (9) (2009) 1844–1851.
[45] T. Tahtouh, F. Halter, C. Caillol, F. Foucher, C. Mounaim-Rousselle, Nonlinear effects of stretch on the flame propagation, in: 4th European Combustion Meeting, Vienna (Austria), 2009, Vienna (Austria), 2009.

[46] F. Halter, T. Tahtouh, C. Mounaïm-Rousselle, Combust. Flame 157 (10) (2010) 1825–1832.
[47] Z. Chen, Combust. Flame (2010), doi:10.1016/j.combustflame.2010.09.001.
[48] Y. Yu, G. Masuya, P.D. Ronney, Proc. Combust. Inst. 27 (1998) 2619–2626.
[49] E. Varea, A. Vandel, V. Modica, F. Corbin, G. Godard, B. Renou, in: 15th International Symposium on Applications of Laser Techniques to Fluid Mechanics, Lisbon, Portugal, 2010.
[50] C.K. Law, Combustion Physics, Cambridge University Press, 2006.
[51] S. Suzuki, K. Abe, Comput. Vis., Graph. Image Process. 30 (1985) 32–46.
[52] A. Razet, Bull. Bureau natl. métrol. 108 (1997) 39–48.
[53] G.R.A. Groot, L.P.H. De Goey, Proc. Combust. Inst. 29 (2) (2002) 1445–1451.
[54] T. Tahtouh, F. Halter, C. Mounaïm-Rousselle, Combust. Flame 156 (9) (2009) 1735–1743.
[55] G.P. Smith, D.M. Golden, M. Frenklach, N.W. Moriarty, B. Eiteneer, M. Goldenberg, C.T. Bowman, R.K. Hanson, S. Song, W.C. Gardiner Jr., V.V. Lissianski, Z. Qin, GRI-Mech Homepage, Gas Research Institute, 1999.
[56] C.T. Bowman, R.K. Hanson, D.F. Davidson, W.C. Gardiner, V. Lissianski, G.P. Smith, D.M. Golden, M. Frenklach, M. Goldenberg, GRI-Mech Homepage, Gas Research Institute, 1994.
[57] G. Broustail, P. Seers, F. Halter, G. Moréac, C. Mounaim-Rousselle, Fuel 90 (1) (2011) 1–6, doi:10.1016/j.fuel.2010.09.021.